

## The moment of initial crystallization captured on functionalized nanoparticles

Hironobu Machida <sup>1✉</sup>, Takeshi Sugahara <sup>2✉</sup> & Izumi Hirasawa<sup>3</sup>

Even if a liquid is cooled below its melting point, the liquid state can be maintained under certain conditions. This state is called supercooling. Spraying fine particles of dry ice or silver iodide induces a phase change from supercooled droplets to ice grains. However, the mechanism by which crystallization seeds diminish supercooling is not well understood. Here, we captured the moment when a cluster, which is the smallest structural unit of a crystal, envelops a silver nanoparticle. As a result of observing the structure of a supercooled aqueous solution of a clathrate hydrate, we found that silver nanoparticles accelerate the formation of clusters, whereas the noble metals palladium, gold and iridium likewise form nanoparticles but do not promote crystallization. Our discoveries elucidate the mechanism of heterogeneous nucleation during a phase change in clathrate hydrates. We anticipate our discovery to be the starting point for the control of supercooling, a technique that can be applied to enhance the production efficiency and quality of manufactured products.

<sup>1</sup>Corporate Engineering Division, Appliances Company, Panasonic Corporation, Moriguchi, Osaka, Japan. <sup>2</sup>Division of Chemical Engineering, Department of Materials Engineering Science, Graduate School of Engineering Science, Osaka University, Toyonaka, Osaka, Japan. <sup>3</sup>Department of Applied Chemistry, Waseda University, Shinjuku-ku, Tokyo, Japan. ✉email: [machida.hi@jp.panasonic.com](mailto:machida.hi@jp.panasonic.com); [sugahara@cheng.es.osaka-u.ac.jp](mailto:sugahara@cheng.es.osaka-u.ac.jp)

Heat storage technology is anticipated to have the potential for the effective use of unused thermal energy currently vented into the environment, such as automobile exhaust heat, factory exhaust heat, and household waste heat<sup>1,2</sup>. There are various technologies for heat storage, of which latent heat stored by phase change at the desired temperature is of particular interest due to its ease of use and low cost<sup>3,4</sup>. Latent heat storage materials have been actively studied since around 1980, but practical examples are currently limited to cold storage boxes for outdoor use and pocket heaters. One major impediment to its practical use is supercooling<sup>5–7</sup>, a phenomenon in which the liquid phase is maintained even when it is cooled below the freezing point. Supercooling phenomena lead to problems such as unreliable heat storage and increased cooling costs. To minimize supercooling, it is important to understand the crystallization mechanism of supercooled aqueous solutions.

Here, we focus on clathrate hydrate crystallization from an aqueous solution. A clathrate hydrate is composed of water and guest molecules. The hydrogen-bonded water molecules surround the guest molecule to form a cage structure<sup>8</sup>. Among clathrate hydrates, the hydrates formed from aqueous solutions of quaternary onium salts have been classified as semiclathrate hydrates<sup>9–11</sup>. Tetra-*n*-butylammonium bromide (TBAB) semiclathrate hydrate has been investigated in the fields of gas separation<sup>12</sup>, as well as thermal storage<sup>13–16</sup>.

We have observed the nanometer-scaled solution structure in supercooled TBAB aqueous solutions<sup>16,17</sup> by applying the freeze-fracture replica method and have elucidated the relationship between the hysteresis phenomenon in recrystallization (called the memory effect) and the residual solution structure after solid dissociation. In both the supercooled aqueous solution and the crystal, granular structures (called clusters) measuring 10–30 nm in diameter are present as a basic structural unit<sup>16–23</sup>. During crystallization, the number density of the clusters significantly increases. Immediately prior to crystallization, the clusters are densely packed in the supercooled aqueous solution<sup>16,17,21,22</sup>. To diminish supercooling, therefore, it is necessary to promote cluster formation and densification. The memory effect contributes considerably to raising the formation temperature of TBAB semiclathrate hydrate and reducing the degree of supercooling. However, it is not sufficient, because few residual solution structures (clusters) can survive long enough, even at a temperature 2 K above the decomposition temperature of TBAB semiclathrate hydrate. The development of chemically and thermodynamically stable materials that promote cluster formation (hereinafter called “crystallization seeds”) is therefore necessary. One example of the prevention of supercooling is seen with artificial rainfall. There are two kinds of rainy clouds: a cold cloud below 273 K and a warm cloud above 273 K<sup>24</sup>. To make it rain artificially in cold clouds, it is necessary to form ice crystallites in a supercooled cloud. The fine silver iodide particles nucleate ice crystallization<sup>24</sup>. It is thought that the lattice constants of the hexagonal form of silver iodide are very similar to those of ice, which is why silver iodide works as a nucleus<sup>24</sup>. However, the mechanism of how crystallization seeds diminish supercooling is not fully known because the crystal structure of seeds is not always similar to that of the crystal nucleated by crystallization seeds<sup>25</sup>. Many researchers have investigated the role of crystallization seeds and the secondary nucleation mechanism induced by crystallization seeds<sup>25–28</sup>.

Here, we reveal the moment of initial crystallization, which is the formation of 10–30 nm clusters encircling silver (Ag) nanoparticles, in the tetra-*n*-butylammonium 3-methylpentanoate (TBA-3MP) and tetra-*n*-butylammonium 2-ethylbutyrate (TBA-2EB) semiclathrate hydrate systems. The synergetic effect of Ag nanoparticles and tetra-*n*-butylammonium fluoride (TBAF) diminishes supercooling to a practicable level during the formation of these semiclathrate hydrates.

## Results and discussion

**Effect of metallic carboxylates with or without TBAF on the degree of supercooling.** Figure 1 shows the degree of supercooling ( $\Delta T_{\text{sup}}$ ) in the formation of TBA-3MP and TBA-2EB semiclathrate hydrates with various metallic carboxylates and/or TBAF added. The decomposition temperature of TBA-3MP semiclathrate hydrate coexisting with TBAF and silver pentanoate (Ag-PA) is  $278.1 \pm 0.2$  K at a mass fraction,  $w_{\text{TBA-3MP}}$ , of 0.42 (Supplementary Fig. 1), which is the same as the reported decomposition temperature of TBA-3MP semiclathrate hydrate without any additives<sup>29</sup>. Without any additives present (Sample #1), a degree of supercooling greater than 10 K is necessary to

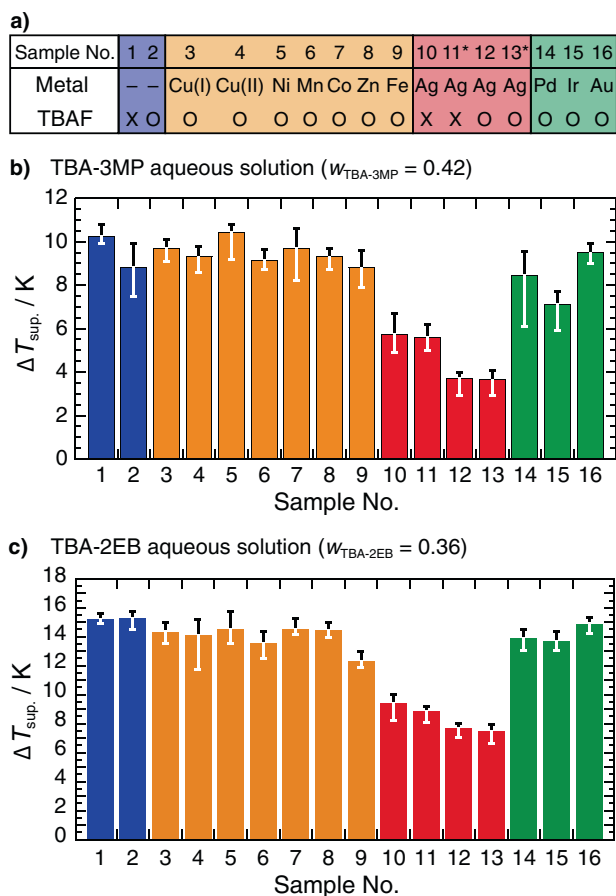


**Fig. 1** Effect of metallic carboxylates on the degree of supercooling. **a** List of samples #1 to #16. The additive(s) was (were) added to the tetra-*n*-butylammonium 3-methylpentanoate (TBA-3MP) and tetra-*n*-butylammonium 2-ethylbutyrate (TBA-2EB) aqueous solution with the mass fractions ( $w_{\text{TBA-3MP}} = 0.42$  and  $w_{\text{TBA-2EB}} = 0.36$ ) at a molar ratio of metal: F: TBA-3MP (or TBA-2EB) = 1: 10: 2000. The symbols O and X stand for “with tetra-*n*-butylammonium fluoride (TBAF)” and “without TBAF”, respectively. All metal species are added as metallic acetates except for samples #1, #2, #11, and #13. In samples #11 and #13, silver pentanoate was used instead of silver acetate. Samples #3–#9 and #14–#16 are other metallic acetates with different valences. **b** Degree of supercooling ( $\Delta T_{\text{sup}}$ ) in the TBA-3MP semiclathrate hydrate formation (decomposition temperature is 278.1 K). **c** Degree of supercooling ( $\Delta T_{\text{sup}}$ ) in the TBA-2EB semiclathrate hydrate formation (decomposition temperature is 283.2 K<sup>43</sup>). The coexistence of silver carboxylate with TBAF yields a small degree of supercooling. All error bars represent standard deviation.

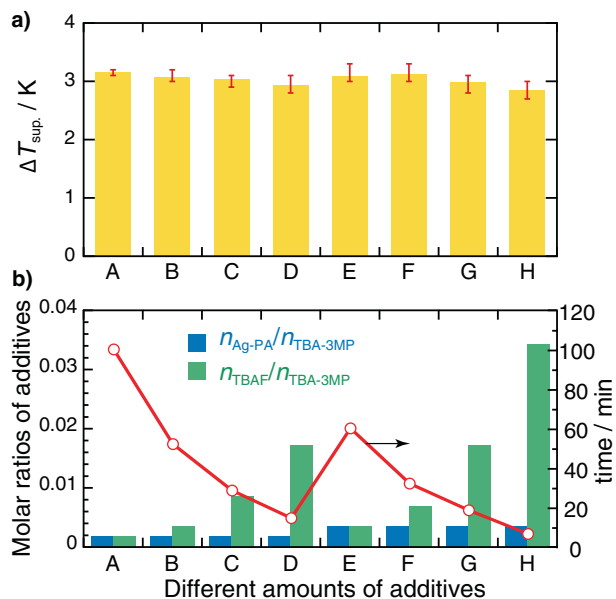


**Fig. 2** Effect of the amount of additives. **a** The degree of supercooling. Error bars represent standard deviation. **b** The time for crystallization to be completed. Ag-PA and TBAF were added as additives to the TBA-3MP aqueous solution with the mass fraction ( $w_{TBA-3MP} = 0.42$ ). The amount ( $n_{TBA-3MP}$ ) of TBA-3MP included in the aqueous solution is 1.4 mmol. The higher the ratio of TBAF was, the faster the crystallization was completed, whereas the degree of supercooling was almost independent of it.

form a TBA-3MP semicathrate hydrate. Even if only TBAF (Sample #2) and a transition-metallic acetate, as well as TBAF (Samples #3-9 and #14-16), were added, the degree of supercooling was little changed. When either silver acetate or Ag-PA was added, the degree of supercooling was brought down to approximately 6 K. Further improvement (approximately 4 K) of the degree of supercooling results from the synergetic effect of silver acetate (or Ag-PA) with TBAF. The synergetic effect of silver carboxylate with TBAF is also similar to that in TBA-2EB aqueous solution. The time required by the end of crystallization of TBA-3MP semicathrate hydrate also depends on the amounts of Ag-PA and TBAF present (Fig. 2b), whereas the degree of supercooling is almost independent of their amounts (Fig. 2a). Why does a combination of silver carboxylates with TBAF effectively diminish supercooling? To elucidate the reasons, we observed nanometer-scaled solution structures in the TBA-3MP aqueous solution using the freeze-fracture replica method. We also investigated the state of metallic species (Ag, palladium (Pd), iridium (Ir), and gold (Au)) in the TBA-3MP aqueous solution by use of X-ray absorption spectra (XAS).

**Microscopic observation of cluster formation.** As mentioned above, in supersaturated or supercooled aqueous solutions, clusters measuring 10–30 nm in diameter are already present. Many researchers have reported the existence of similar clusters in various experiments<sup>16–23,30,31</sup>. To be able to diminish supercooling, it is essential to promote cluster formation and its densification at higher temperatures. Shown in Fig. 3a are scanning transmission electron microscopic (STEM) images of the replica films prepared from sample solutions #1, 2, 11, and 13 (listed in Fig. 1a) at 281 K, 279 K, 277 K, and 275 K. In the TBA-3MP aqueous solution (Sample #1) without silver pentanoate (Ag-PA) nor TBAF, few 10–30 nm clusters exist at 279 K and 281 K higher than the equilibrium temperature of TBA-3MP semicathrate hydrate. It was very difficult to find a number of clusters,

although each STEM image included several. On decreasing the temperature, the number of clusters gradually increases and the clusters begin to agglomerate to 80–100 nm at 275 K. When TBAF was added (Sample #2), the behavior of 10–30 nm cluster formation was similar to that seen in Sample solution #1.

We have already reported that, when Ag-PA was added to the TBA-3MP aqueous solution (Sample #11), Ag nanoparticles measuring approximately 5 nm appeared in the solution<sup>32</sup>. X-ray diffraction, energy-dispersive X-ray spectroscopy (EDX), and electron energy loss spectroscopy analyses showed the formed nanoparticles to be metallic silver<sup>32</sup>. In spite of the presence of Ag nanoparticles, the behavior of 10–30 nm cluster formation in the Sample solution #11 was similar to that of Sample solutions #1 and #3. Similar Ag nanoparticles appear in not only STEM images of Sample solution #11 but also in #13. In Sample solution #13, to which both Ag-PA and TBAF had been added, a certain number of 10–30 nm clusters were already present at 281 K. The number of these clusters significantly increased on lowering the temperature. Finally, at 275 K, the 10–30 nm clusters were densely packed. Shown in Fig. 3b and Fig. 3c are the STEM image of the replica films (same as the ones in “13-a” of Fig. 3a) prepared from Sample solution #13 at 281 K and the EDX charts at some points in Fig. 3b, respectively. In Fig. 3b, an Ag nanoparticle of 5 nm or less in diameter was observed as a black spot inside each 10–30 nm cluster. The EDX charts reveal that Ag nanoparticles are made of metallic silver<sup>32</sup>. Figure 3b is of particular interest: it is a STEM image of the replica film prepared from the TBA-3MP aqueous solution (Sample #13) kept at 281 K. Despite the temperature being higher than the equilibrium temperature of TBA-3MP semicathrate hydrate, a relatively large number of 10–30 nm clusters were generated. Most of them appear to include an Ag nanoparticle of 5 nm or less as a core. A comparison between sample solutions #11 and #13 suggests the coexistence of Ag nanoparticles and fluoride anions leads to the promotion of cluster formation. The STEM image in Fig. 3b has been taken at the precise moment of cluster formation.

### Why did only Ag, but not Pd, Ir, or Au nanoparticles diminish supercooling?

We have already reported the formation of corresponding metal nanoparticles of Pd, Ir, and Au<sup>32</sup>. In either system, carboxylate ion is thought to contribute to preventing metal nanoparticles from aggregating due to steric hindrance. To understand the unique nature of Ag and the chemical forms of Ag on an atomic or molecular level, we measured the XAS of Ag, Pd, Ir, and Au. XAS is a tool for gaining information on the type of neighboring atoms, which can be usually deduced by comparison of the XAS spectrum of the sample with those of suitable reference compounds. Shown in Figs. 4a and b are the Ag *K*-edge X-ray absorption near-edge structure (XANES) spectra of the sample solutions (#13 measured at 273 K and 293 K) along with the reference compound silver fluoride (AgF), Ag-PA, silver nitrate (AgNO<sub>3</sub>), Ag foil, silver monoxide (AgO), and silver(I) oxide (Ag<sub>2</sub>O). On comparing them at the rising-edge region of 25.50–25.51 keV, the rising-edge behavior of the sample solutions measured at 273 K and 293 K was somewhat similar to that of AgF, AgNO<sub>3</sub>, and Ag-PA, whereas it was different from that of Ag foil, AgO, and Ag<sub>2</sub>O. At the energy side higher than the absorption edge, the Ag *K*-edge XANES spectrum (orange) of sample solution #13 measured at 293 K was somewhat flat. It appears that Ag has no interaction with any specific atoms in the sample solution. On decreasing the temperature to 273 K, the XANES spectrum (red) changed and showed a peak at 25.51 keV. The spectral shape is similar to that of AgF in an aqueous solution. These XANES spectra suggest that Ag exists without any preferential binding partner at 293 K, but, at 273 K, the

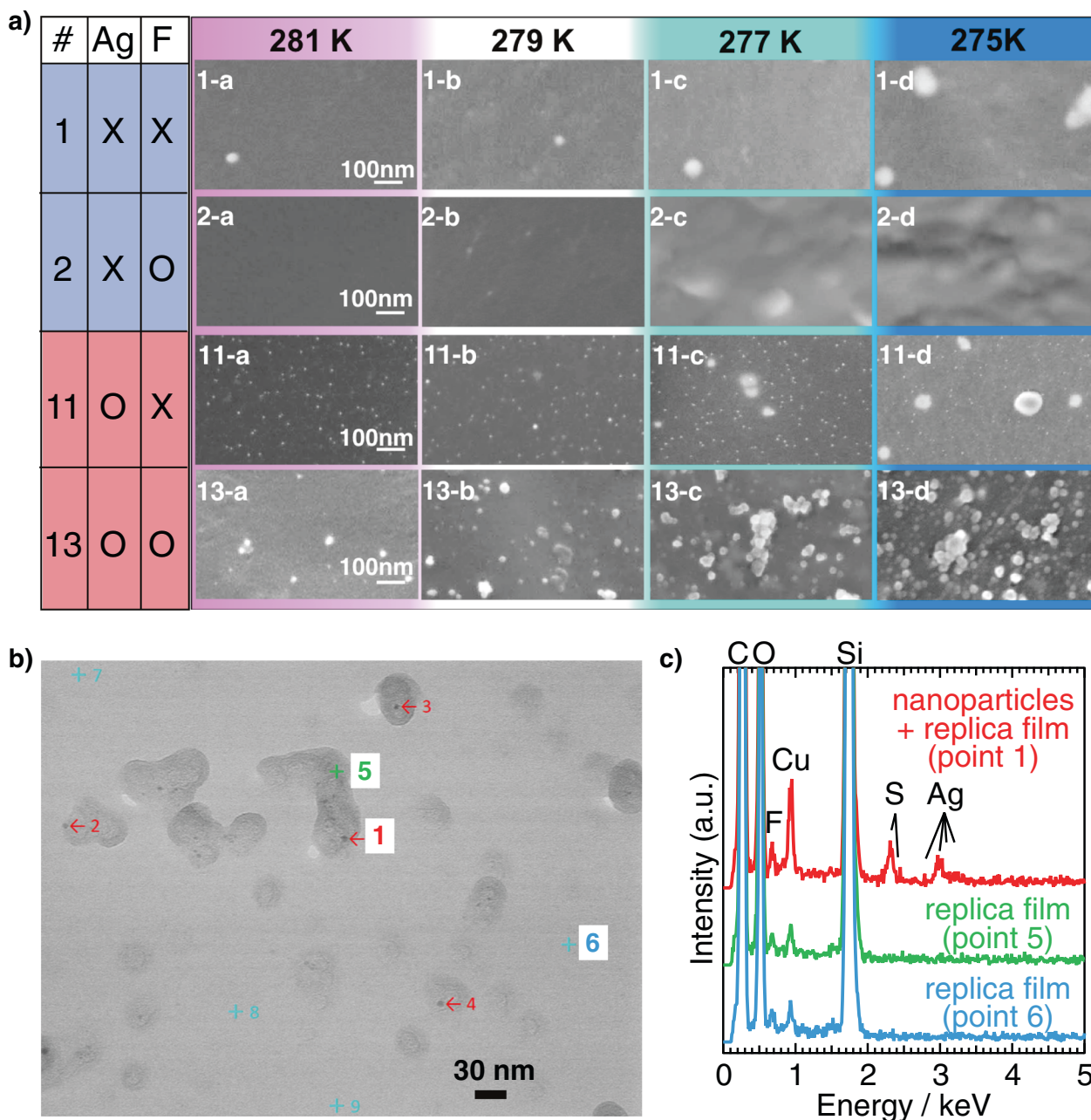


**Fig. 3 Cluster formation of semiclathrate hydrate around silver nanoparticles. a** HAADF-STEM image of replica films prepared from samples #1, #2, #11, and #13 of TBA-3MP aqueous solutions listed in Fig. 1a. A number of silver nanoparticles smaller than 10 nm were observed in samples #11 and #13. **b** SE-STEM image (different area) of the same replica film as “13-a” in **a**. EDX measurements were performed at points 1-9. **c** Typical EDX charts at points 1, 5, and 6 in **b**. EDX charts of points 1-4 reveal the existence of silver nanoparticles incorporated in replica film. Like enclosing silver nanoparticles, clusters of 10-30 nm were formed.

interaction between Ag and fluorine, in addition to Ag and pentanoate, strengthens. We attempted to analyze the Fourier-transformed-extended X-ray absorption fine structure (FT-EXAFS) region of Ag. However, the S/N ratio was so low that, due to insufficient Ag concentration, we could not obtain any meaningful data. The Pd *K*-edge, Ir *L<sub>III</sub>*-edge, and Au *L<sub>III</sub>*-edge XANES, and FT-EXAFS spectra of the sample solutions #14, #15, and #16 are shown in Fig. 4c, d, and e along with possible reference compounds. Both the XANES and FT-EXAFS spectra reveal that the environment of a Pd, Ir, or Au atom is similar to that of their respective metal acetates: in other words, Pd, Ir, and Au are present as acetate-coordinated complexes in the sample solutions. These XAS results indicate an answer to the question as

to why Ag effectively diminishes supercooling, but Pd, Ir, and Au do not. Since Pd, Ir, and Au ions are divalent, tetravalent, and trivalent, respectively, they are coordinated with two, four, and three acetate ions. These multiple acetate ions prevent other ions from approaching the Pd, Ir, and Au atoms. Since the Ag ion is monovalent, however, there is just enough space for other ions to approach Ag, even if it is coordinated with an acetate ion. In Sample solution #13, fluoride ion is present as a counter anion to the TBA cation. Therefore, with a decrease in temperature, the spectral element of AgF increases in addition to that of Ag-PA in the XANES spectrum of Sample solution #13. The approach of fluoride ions to Ag nanoparticles yields an enriched area of fluoride ions around the Ag nanoparticles. Local enrichment of

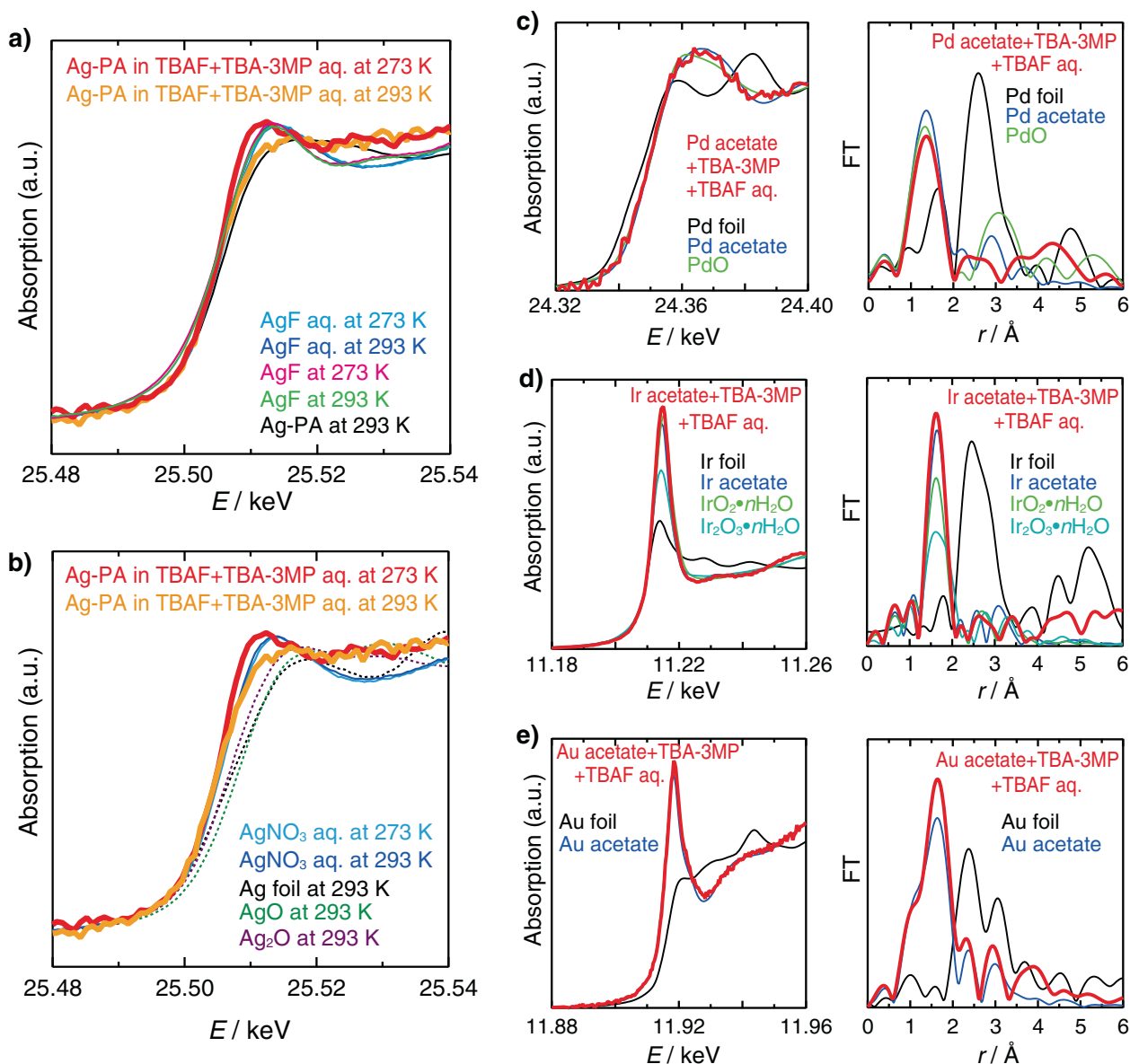


**Fig. 4** XAS spectra. **a** Comparison of Ag K-edge XANES spectra of Ag-PA in TBAF + TBA-3MP aqueous solutions at 273 K and 293 K with AgF, AgF aqueous solution, and Ag-PA. XANES spectrum of Ag species in TBAF + TBA-3MP aqueous solutions at 293 K has relatively no features. At 273 K, it approaches that of AgF in the aqueous solution. **b** Comparison of Ag K-edge XANES spectra of Ag-PA in TBAF + TBA-3MP aqueous solutions at 273 K and 293 K with other possible Ag compounds. **c** Pd K-edge XANES and FT-EXAFS spectra at 293 K. **d** Ir  $L_{III}$ -edge XANES and FT-EXAFS spectra at 293 K. **e** Au  $L_{III}$ -edge XANES and FT-EXAFS spectra at 293 K.

fluoride ions increases the probability of formation of 10–30 nm TBAF (or TBAF + TBA-3MP mixed) semicathrate hydrate clusters around Ag nanoparticles at 281 K (as shown in Fig. 3b) since Ag nanoparticles also effectively diminish supercooling in the TBAF semicathrate hydrate formation (Fig. 5). The 10–30 nm clusters of the semicathrate hydrate act as crystallization seeds for TBA-3MP semicathrate hydrate formation due to the similarity (tetragonal lattice)<sup>11,33,34</sup> of the two crystal structures (Supplementary Table 1 and Supplementary Fig. 2). It follows that the TBA-3MP semicathrate hydrate can be formed at a relatively small degree of supercooling.

To summarize this study: we have reported that Ag nanoparticles act to diminish supercooling under the coexistence of TBAF during the formation of TBA-3MP and TBA-2EB semicathrate hydrates and have elucidated the mechanism, which is the promotion of the formation of 10–30 nm clusters

around Ag nanoparticles, through STEM observation using the freeze-fracture replica method and XAS. Furthermore, neither Ag nanoparticles nor TBAF has an effect on diminishing supercooling alone. The present results suggest a useful strategy for diminishing supercooling of TBA salt semicathrate hydrate formation when used as heat storage materials. A role for Ag compounds in diminishing supercooling and a possible mechanism can also be proposed that does not depend on the similarity of the crystal structure to Ag compounds.

## Methods

**Samples.** Tetra-*n*-butylammonium-3-methylpentanoate (TBA-3MP) and Tetra-*n*-butylammonium-2-ethylbutyrate (TBA-2EB) were synthesized by aqueous neutralization of tetra-*n*-butylammonium hydroxide (TBAOH, Tokyo Chemical Industry) with 3-methylpentanoic acid (Tokyo Chemical Industry) and 2-ethylbutyric acid (Tokyo Chemical Industry), respectively. The resultant aqueous solutions were completely dried under vacuum at 40 °C to obtain TBA-3MP and

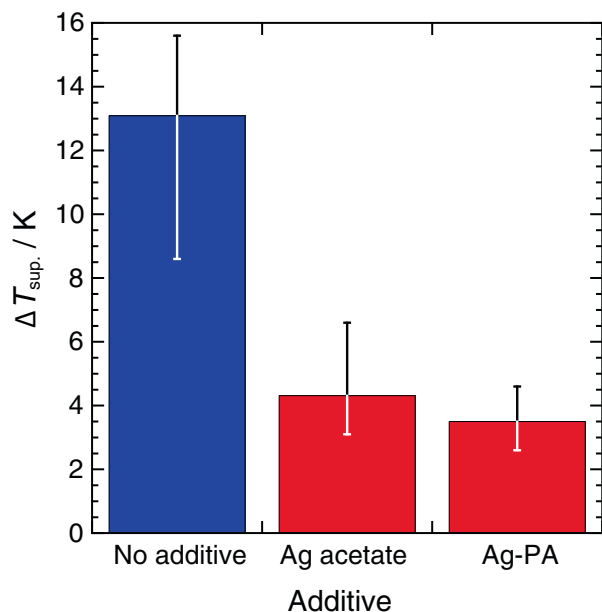


**Fig. 5 Effect of Ag carboxylates on the degree of supercooling in the TBAF semicathrate hydrate (SCH) formation.** The equilibrium temperature of TBAF SCH is 300.55–300.75 K<sup>11,44</sup>. Error bars represent standard deviation.

TBA-2EB. The obtained products were confirmed by <sup>1</sup>H NMR. The purity of the synthesized TBA-3MP or TBA-2EB was virtually the same as that of TBA-OH (on a water-free basis) and 3-methylpentanoic acid or 2-ethylbutyric acid. The majority of the impurities were tri-*n*-butylamine, 1-bromobutane, and KBr that were originally present in the TBA-OH aqueous solution. In the NMR and ion chromatographic (Thermo Fisher Scientific, Integriion HPIC) analyses, the concentrations of these expected impurities, as well as the others, were below the detection limits. TBA-3MP (mass fraction  $w_{\text{TBA-3MP}} = 0.42$ ) and TBA-2EB (mass fraction  $w_{\text{TBA-2EB}} = 0.36$ ) aqueous solutions were prepared. Close to equimolar amounts of silver nitrate (Fujifilm Wako Pure Chemical Corporation) and pentanoic acid (Tokyo Chemical Industry) were added to water under dark conditions. The addition of sodium hydroxide (Tokyo Chemical Industry) aqueous solution for neutralization led to the precipitation of silver pentanoate (Ag-PA). This precipitate was filtered, washed, and dried. Ag-PA and tetra-*n*-butylammonium fluoride (TBAF, Tokyo Chemical Industry) solution was added to TBA-3MP aqueous solution ( $w_{\text{TBA-3MP}} = 0.42$ ) at a molar ratio of Ag: F: TBA-3MP (or TBA-2EB) = 1: 10: 2000. The addition of TBAF supplementarily improves the solubility of Ag-PA. Other sample solutions of the metallic acetates listed in Fig. 1a were also prepared at the same molar ratio. They were then stirred ultrasonically and placed under diffuse sunlight and a fluorescent room lamp (Panasonic, FHF32EX-N-H) for one day. The wavelength and energy irradiated to the samples were measured with an illuminance spectrophotometer (Konica Minolta, CL-500A). The result (not shown) indicated low optical energy in the ultraviolet region below 400 nm.

**Structural observation in aqueous solution.** A freeze-fracture replica method<sup>16,21,22,32,35–42</sup> was used for structural observation in aqueous solution. First, a droplet (1  $\mu\text{L}$ ) of the aqueous solution at the desired temperature was injected into a platinum cell with an internal diameter of 1 mm. Next, the platinum cell containing the droplet was dipped into liquid 2-methyl butane at its melting point (113 K). This caused the droplet to vitrify. The vitrified droplet was then cut in a vacuum chamber (JEOL, EM-19501 JFD-V) maintained at approximately 80 K to expose the cut surface. When the solution structures and the nanoparticles are present in an aqueous solution, irregularities reflecting these structures appear on the cut surface. To replicate these irregularities, carbon was vapor-deposited on the cut surface immediately after cutting the vitrified droplet. The vitrified droplet was then dissolved in pure water to obtain an approximately 4 nm-thick carbon replica film. The obtained replica film was picked up on a 200-mesh copper grid (VECO, square type). We prepared at least two replica films under a condition. For each, more than 10 fields were observed using an SEM (Carl Zeiss, Ultra plus, acceleration voltage: 2 kV, detector: InLens) or STEM (Hitachi, HD-2700, acceleration voltage: 200 kV, detector: secondary electron detector (SE) or High angle annular dark-field (HAADF)). The metal nanoparticles remaining in the replica film were analyzed via EDX (EDAX, TEAM, STEM attached, acceleration voltage: 200 kV). In Fig. 3c, the copper originates in the mesh used for SEM observation. The EDX peak of the Si component was also detected as an analysis point outside the Ag nanoparticles. There was no sulfur in the chemicals used in this study. Sulfur

derived from rubber washers might have reacted with Ag nanoparticles being kept under dry conditions before EDX measurement.

**Measurement of the degree of supercooling.** Aliquots of approximately 1 g of the sample solutions (Fig. 1a) were introduced into glass vials. A T-type thermocouple was placed on the outside of the bottom of each glass vial. All the glass vials were placed in a thermostatic bath (Espec, SU-241). The bath was programmed to hold the temperature at 283 K for 60 min and then cool down at 0.05 K min<sup>-1</sup> from 283 K to 263 K. The onset temperature and offset time of the exothermic peak derived from crystallization was determined as the crystallization temperature and the time for crystallization to be completed, respectively. The difference between the crystallization and equilibrium temperatures was taken as the degree of supercooling. These measurements were repeated 14 times and the average degree of supercooling was calculated.

**XAS measurements.** XAS measurements in the TBA-3MP aqueous solutions including Ag-PA or other metal acetates (palladium (Pd), iridium (Ir), and gold (Au)) with TBAF were performed at the beamline (BL) 07 SAGA-Light Source at the Kyushu Synchrotron Light Research Center (For Ag and Pd systems) and the BL 9A Photon Factory at the Institute of Materials Structure Science, High Energy Accelerator Research Organization, KEK (for Ir and Au systems). The reason that two different synchrotron radiation facilities were utilized was due to limits on available time at each. At the BL 07 SAGA-Light Source, the measurements of Ag K-edge and Pd K-edge X-ray absorption near-edge structure (XANES) and extended X-ray absorption fine structure (EXAFS) spectra were performed at 273 K and 293 K using a Si(220) double crystal monochromator and an ionization chamber. The data were recorded in transmission mode with an Ar and Ar + Kr (75:25) gas mixture (before and after samples, respectively). At the BL 9A Photon Factory, the measurements of Ir L<sub>III</sub>-edge and Au L<sub>III</sub>-edge XANES and EXAFS spectra were performed at 293 K using a Si(111) water-cooled double crystal monochromator. The data were recorded in fluorescent X-ray yield mode using a multi Ge solid-state detector (Ge-SSD).

#### Data availability

The data that support the findings of this study are available from the corresponding authors upon reasonable request.

Received: 20 October 2020; Accepted: 26 May 2021;

Published online: 18 June 2021

#### References

1. Kaizawa, A. et al. Thermal and flow behaviors in heat transportation container using phase change material. *Energy Convers. Manage.* **49**, 698–706 (2008).
2. Kürklü, A., Wheldon, A. & Hadley, P. Mathematical modelling of the thermal performance of a phase-change material (PCM) store: Cooling cycle. *Appl. Therm. Eng.* **16**, 613–623 (1996).
3. Mongibello, L., Capezzuto, M. & Graditi, G. Technical and cost analyses of two different heat storage systems for residential micro-CHP plants. *Appl. Therm. Eng.* **71**, 636–642 (2014).
4. Gu, Z., Liu, H. & Li, Y. Thermal energy recovery of air conditioning system – heat recovery system calculation and phase change materials development. *Appl. Therm. Eng.* **24**, 2511–2526 (2004).
5. Miyasaka, E. et al. Effect of ultrasonic irradiation on nucleation phenomena in a Na<sub>2</sub>HPO<sub>4</sub>•12H<sub>2</sub>O melt being used as a heat storage material. *Ultrason. Sonochem.* **13**, 308–312 (2006).
6. Wei, L. & Ohsasa, K. Supercooling and solidification behavior of phase change material. *ISIS Int.* **50**, 1265–1269 (2010).
7. Muthoka, M. J., Xuelai, Z. & Xiaofeng, X. Experimental investigation on supercooling, thermal conductivity and stability of nanofluid based composite phase change material. *J. Energy Storage* **17**, 47–55 (2018).
8. Sloan, E. D. & Koh, C. A. *Clathrate Hydrates of Natural Gases*. 3rd edn. (Taylor & Francis-CRC Press, Boca Raton, 2008).
9. Fowler, D. L. et al. Some unusual hydrates of quaternary ammonium salts. *J. Am. Chem. Soc.* **62**, 1140–1142 (1940).
10. Jeffrey, G. A. *Inclusion Compounds* (eds. Atwood, J. L., Davies, J. E. D., MacNicol, D. D.) Vol. 1, 135–190 Chapter 5 (Academic Press, London, 1984).
11. Dyadin, Y. A. & Udachin, K. A. Clathrate polyhydrates of peralkylonium salts and their analogs. *J. Struct. Chem.* **28**, 394–432 (1987).
12. Hashimoto, H. et al. Structure-driven CO<sub>2</sub> selectivity and gas capacity of ionic clathrate hydrates. *Sci. Rep.* **7**, 17216 (2017).
13. Fukushima, S. et al. Development of high-density cold latent heat with clathrate hydrate. *NKK Technical Rep.* **166**, 65–70 (1999).
14. Oyama, H. et al. Phase diagram, latent heat, and specific heat of TBAB semicathrate hydrate crystals. *Fluid Phase Equilib.* **234**, 131–135 (2005).

15. Rodionova, T. V. et al. Calorimetric and structural studies of tetrabutylammonium bromide ionic clathrate hydrates. *J. Phys. Chem. B* **117**, 10677–10685 (2013).
16. Machida, H., Sugahara, T. & Hirasawa, I. Memory effect in tetra-*n*-butyl ammonium bromide semiclathrate hydrate reformation: the existence of solution structures after hydrate decomposition. *CrystEngComm* **20**, 3328–3334 (2018).
17. Machida, H. et al. Calorimetric and small-angle X-ray scattering studies on the memory effect in the tetra-*n*-butylammonium bromide semiclathrate hydrate system. *J. Cryst. Growth* **533**, 125476 (2020).
18. Mullin, J. W. & Leci, C. L. Evidence of molecular cluster formation in supersaturated solutions of citric acid. *Phil. Mag.* **19**, 1075–1077 (1969).
19. Cussler, E. L. Cluster diffusion in liquids. *AIChE J.* **26**, 43–51 (1980).
20. Larson, M. A. & Garside, J. Solute clustering in supersaturated solutions. *Chem. Eng. Sci.* **41**, 1285–1289 (1986).
21. Ohgaki, K., Hirokawa, N. & Ueda, M. Heterogeneity in aqueous solutions: electron microscopy of citric acid solutions. *Chem. Eng. Sci.* **47**, 1819–1823 (1991).
22. Ueda, M. et al. Change in microstructure of an aqueous citric acid solution under crystallization. *J. Crystal Growth* **156**, 261–266 (1995).
23. Matsushita, Y. et al. Time-resolved X-ray tracking of expansion and compression dynamics in supersaturating ion-networks. *Sci. Rep.* **5**, 17647 (2015).
24. Mason, B. J. Design and evaluation of large-scale rain-making experiments. *Nature* **175**, 448–451 (1955).
25. Allahyarov, E. et al. Crystallization seeds favour crystallization only during initial growth. *Nat. Comm.* **6**, 7110 (2015).
26. Loh, N. D. et al. Multistep nucleation of nanocrystals in aqueous solution. *Nat. Chem.* **9**, 77–82 (2017).
27. Yousuf, M. & Frawley, P. J. Experimental evaluation of fluid shear stress impact on secondary nucleation in a solution crystallization of paracetamol. *Cryst. Growth Des.* **18**, 6843–6852 (2018).
28. Kobari, M., Kubota, N. & Hirasawa, I. Simulation of metastable zone width and induction time for a seeded aqueous solution of potassium sulfate. *J. Cryst. Growth* **312**, 2734–2739 (2010).
29. Nakayama, H. & Torigata, S. Hydrates of organic compounds. VIII. The effect of carboxylate anions on the formation of clathrate hydrates of tetrabutylammonium carboxylates. *Bull. Chem. Soc. Jpn.* **57**, 171–174 (1984).
30. Yamazaki, T. et al. Two types of amorphous protein particles facilitate crystal nucleation. *Proc. Natl Acad. Sci. USA* **114**, 2154–2159 (2017).
31. Jehannin, M., Rao, A. & Cölfen, H. New horizons of nonclassical crystallization. *J. Am. Chem. Soc.* **141**, 10120–10136 (2019).
32. Machida, H., Sugahara, T. & Hirasawa, I. Preparation of dispersed metal nanoparticles in the aqueous solution of metal carboxylate and the tetra-*n*-butylammonium carboxylate. *J. Cryst. Growth* **514**, 14–20 (2019).
33. McMullan, R. & Jeffrey, G. A. Hydrates of the tetra-*n*-butyl and tetra-*i*-amyl quaternary ammonium salts. *J. Chem. Phys.* **31**, 1231–1234 (1959).
34. Hashimoto, H. et al. CO<sub>2</sub> capture from flue gas based on tetra-*n*-butylammonium fluoride hydrates at near ambient temperature. *ACS Omega* **5**, 7115–7123 (2020).
35. Ohgaki, K. et al. Solute clusters in aqueous citric acid solutions. *Chem. Eng. Sci.* **46**, 3283–3287 (1991).
36. Machida, H., Sugahara, T. & Hirasawa, I. Relationship between supercooling stability and solution structure in sodium acetate aqueous solution. *J. Cryst. Growth* **475**, 295–299 (2017).
37. Chalcraft, J. P. & Bullivant, S. An interpretation of liver cell membrane and junction structure based on observation of freeze-fracture replicas of both sides of the fracture. *J. Cell. Biol.* **47**, 49–60 (1970).
38. Heuser, J. E. Quick-freeze, deep-etch method of preparing samples for 3-D electron microscopy. *Trends Biochem. Sci.* **6**, 64–68 (1980).
39. Zasadzinski et al. Scanning tunneling microscopy of freeze-fracture replicas of biomembranes. *Science* **239**, 1013–1015 (1988).
40. Fujimoto, K. Freeze-fracture replica EM combined with SDS digestion for cytochemical labeling of integral membrane proteins – application to the immunogold labeling of intercellular junctional complexes. *J. Cell Sci.* **108**, 3443–3449 (1995).
41. Murakami, M., Tanaka, A. & Ohgaki, K. Preparation of replica film using mixed hydrocarbon plasma. *Appl. Plasma Sci.* **5**, 90–93 (1997).
42. Ohgaki, K. et al. Physicochemical approach to nanobubble solutions. *Chem. Eng. Sci.* **65**, 1296–1300 (2010).
43. Sugahara, T. et al. Thermodynamic properties of tetra-*n*-butylammonium 2-ethylbutyrate semiclathrate hydrate for latent heat storage. *Int. J. Refrigeration* **106**, 113–119 (2019).
44. Sakamoto, J. et al. Thermodynamic and Raman spectroscopic studies on hydrogen + tetra-*n*-butyl ammonium fluoride semi-clathrate hydrates. *Chem. Eng. Sci.* **63**, 5789–5794 (2008).

## Acknowledgements

H.M., T.S., and I.H. gratefully acknowledge financial support from the Thermal Management Materials and Technology Research Association (TherMAT) project, commissioned by the New Energy and Industrial Technology Development Organization (NEDO). T.S. was supported by JSPS Kakenhi (Grant no. JP18K05032). We gratefully thank Dr. S. Muromachi and Dr. N. Tenma, of the National Institute of Advanced Industrial Science and Technology (AIST) for the XRD measurements and analyses. We also thank Kaneka Techno Research Corporation and Toray Research Center, Inc., respectively, for technical assistance with the STEM and the XAS experiments.

## Author contributions

H.M., T.S. and I.H. conceived the research idea. H.M. performed the measurements of the degree of supercooling and analyzed the XAS data. H.M. and T.S. summarized the research results and wrote the manuscript after discussion with and obtaining input from all the coauthors.

## Competing interests

The authors declare no competing interests.

## Additional information

**Supplementary information** The online version contains supplementary material available at <https://doi.org/10.1038/s43246-021-00171-w>.

**Correspondence** and requests for materials should be addressed to H.M. or T.S.

**Peer review information** *Communications Materials* thanks the anonymous reviewers for their contribution to the peer review of this work. Primary Handling Editor: Aldo Isidori. Peer reviewer reports are available.

**Reprints and permission information** is available at <http://www.nature.com/reprints>

**Publisher's note** Springer Nature remains neutral with regard to jurisdictional claims in published maps and institutional affiliations.

 **Open Access** This article is licensed under a Creative Commons Attribution 4.0 International License, which permits use, sharing, adaptation, distribution and reproduction in any medium or format, as long as you give appropriate credit to the original author(s) and the source, provide a link to the Creative Commons license, and indicate if changes were made. The images or other third party material in this article are included in the article's Creative Commons license, unless indicated otherwise in a credit line to the material. If material is not included in the article's Creative Commons license and your intended use is not permitted by statutory regulation or exceeds the permitted use, you will need to obtain permission directly from the copyright holder. To view a copy of this license, visit <http://creativecommons.org/licenses/by/4.0/>.

© The Author(s) 2021